

Auto-correlation Function Analysis of Scattered Light Intensity at Different Scattering Angles

Yong Sun*

October 19, 2018

Abstract

In this work, the effects of the scattering angle on the nonexponentiality of the normalized time auto-correlation function of the scattered light intensity $g^{(2)}(\tau)$ are investigated using dilute Poly(*N*-isopropylacrylamide) microgel and standard polystyrene latex samples in dispersion respectively. The results show that the influences of the scattering angle on the deviation between an exponentiality and $g^{(2)}(\tau)$ are small. With the assistance of the simulated data of $g^{(2)}(\tau)$, the effects of the particle size distribution and scattering angle on the deviation between an exponentiality and $g^{(2)}(\tau)$ are explored. The analysis reveals that the nonexponentiality of $g^{(2)}(\tau)$ is determined by the particle size distribution and scattering angle. In general, the influences of the particle size distribution are small on the nonexponentiality of $g^{(2)}(\tau)$ and very large on the initial slope of the logarithm of $g^{(2)}(\tau)$ and the effects of the scattering angle are determined by the particle size distribution and mean particle size. Under some conditions, the deviation between an exponentiality and $g^{(2)}(\tau)$ is greatly influenced by the scattering angle. The values of the apparent hydrodynamic radius are also determined by the particle size distribution and scattering angle. The apparent hydrodynamic radius and its distribution obtained using the cumulants method are different from the hydrodynamic radius and its distribution.

1 INTRODUCTION

Light scattering is a widely used technique to measure the properties of particles in colloidal dispersion systems. One of the main applications of the dynamic light scattering (DLS) technique is to measure the sizes of spherical particles in liquid suspension. The standard method of cumulants [1–4] has been used to measure the hydrodynamic radius, or more strictly apparent hydrodynamic radius $R_{h,app}$ [5] of particles from the normalized time auto-correlation function of the scattered light intensity $g^{(2)}(\tau)$ with the assistance of the Einstein-Stokes relation, where τ is the delay time. In order to obtain the effective diffusion

*Email: ysun2002h@yahoo.com.cn

coefficient [6] or the apparent hydrodynamic radius [5] to detect small polydispersities for large particles, DLS technique is endeavored to use at different scattering angles.

In the previous work [7–9], the particle size information included in the static and dynamic light scattering data and the influences of particle size distribution on the deviation between an exponentiality and $g^{(2)}(\tau)$ at a scattering angle of 30° have been explored. The particle size distributions obtained using different techniques have been compared. In this work, the effects of the scattering angle on the nonexponentiality of $g^{(2)}(\tau)$ are investigated using dilute Poly(*N*-isopropylacrylamide) microgel and standard polystyrene latex samples in dispersion respectively. The results show that the effects of the scattering angle on the deviation between an exponentiality and $g^{(2)}(\tau)$ are small. Since the method of cumulants measures the particle size distribution from the nonexponentiality of $g^{(2)}(\tau)$ at a single scattering angle, the simulated data were thus used to explore the effects of the particle size distribution on the difference between them at different scattering angles. The analysis reveals that the deviation between an exponentiality and $g^{(2)}(\tau)$ is determined by the particle size distribution and scattering angle. In general, the influences of the particle size distribution are small on the nonexponentiality of $g^{(2)}(\tau)$ and very large on the initial slope of the logarithm of $g^{(2)}(\tau)$ and the effects of the scattering angle are determined by the particle size distribution and mean particle size. Under some conditions, the deviations between an exponentiality and $g^{(2)}(\tau)$ are greatly influenced by the scattering angle. The values of the apparent hydrodynamic radius are also determined by the particle size distribution and scattering angle. The apparent hydrodynamic radius and its distribution obtained using the cumulants method are different from the hydrodynamic radius and its distribution.

2 THEORY

When the Rayleigh-Gans-Debye (RGD) approximation is valid, the normalized time auto-correlation function of the electric field of the scattered light $g^{(1)}(\tau)$ for dilute poly-disperse homogeneous spherical particles in dispersion is given by

$$g^{(1)}(\tau) = \frac{\int_0^\infty R_s^6 P(q, R_s) G(R_s) \exp(-q^2 D \tau) dR_s}{\int_0^\infty R_s^6 P(q, R_s) G(R_s) dR_s}, \quad (1)$$

where R_s is the static radius, D is the diffusion coefficient, $q = \frac{4\pi}{\lambda} n_s \sin \frac{\theta}{2}$ is the scattering vector, λ is the wavelength of the incident light in vacuo, n_s is the solvent refractive index, θ is the scattering angle, $G(R_s)$ is the number distribution of particle sizes and the form factor $P(q, R_s)$ is

$$P(q, R_s) = \frac{9}{q^6 R_s^6} (\sin(qR_s) - qR_s \cos(qR_s))^2. \quad (2)$$

From the Einstein-Stokes relation

$$D = \frac{k_B T}{6\pi\eta_0 R_h}, \quad (3)$$

where η_0 , k_B and T are the viscosity of the solvent, Boltzmann's constant and absolute temperature respectively, the hydrodynamic radius R_h can be obtained.

Traditionally the cumulants is a standard method to measure the particle size distribution from the DLS data $g^{(2)}(\tau)$. In this work, the following equation was used to analyze the DLS data to the second moment

$$g^{(2)}(\tau) = 1 + \beta \exp(-2\langle\Gamma\rangle\tau) (1 + \mu_2\tau^2) \quad (4)$$

where $\langle\Gamma\rangle = q^2 D_e(q)$ is the average decay rate, $D_e(q)$ is the effective diffusion coefficient, μ_2 is the second moment and β is a constant that depends on the experimental geometry for a given experimental measurement. The apparent hydrodynamic radius $R_{h,app}$ can be obtained from $D_e(q)$

$$R_{h,app} = \frac{k_B T}{6\pi\eta_0 D_e}. \quad (5)$$

The relative width of the apparent hydrodynamic radius distribution is [10]

$$\frac{Width}{R_{h,app}} = \frac{\sqrt{\mu_2}}{\langle\Gamma\rangle}. \quad (6)$$

If the first cumulant is used, the value of the apparent hydrodynamic radius $R_{h,app}$ at given scattering angle and delay time τ can be calculated directly using the static particle size information and the relationship between the static and hydrodynamic radii. If the DLS data during the delay time range τ_1 and τ_2 are chosen to obtain $R_{h,app}$ at a given scattering angle, the average value of apparent hydrodynamic radius can be calculated using the following equation

$$R_{h,app} \left(e^{-\frac{q^2 k_B T \tau_1}{6\pi\eta_0 R_{h,app}}} - e^{-\frac{q^2 k_B T \tau_2}{6\pi\eta_0 R_{h,app}}} \right) = \frac{\int_0^\infty R_h R_s^6 P(q, R_s) G(R_s) \left(e^{-\frac{q^2 k_B T \tau_1}{6\pi\eta_0 R_h}} - e^{-\frac{q^2 k_B T \tau_2}{6\pi\eta_0 R_h}} \right) dR_s}{\int_0^\infty R_s^6 P(q, R_s) G(R_s) R_s dR_s}. \quad (7)$$

3 EXPERIMENT

The SLS and DLS data were measured using the instrument built by ALV-Laser Vertriebsgesellschaft m.b.H (Langen, Germany). It utilizes an ALV-5000 Multiple Tau Digital Correlator and a JDS Uniphase 1145P He-Ne laser to provide a 23 mW vertically polarized laser at wavelength of 632.8 nm.

In this work, two kinds of samples were used. One is PNIPAM submicron spheres and the other is standard polystyrene latex spheres. The samples used in this work have been detailed before [7]. The four PNIPAM microgel samples

PNIPAM-0, PNIPAM-1, PNIPAM-2 and PNIPAM-5 were named according to the molar ratios n_B/n_N of cross-linker N, N' -methylenebisacrylamide over N -isopropylacrylamide. The sulfate polystyrene latex with a normalized mean radius of 33.5 nm and surfactant-free sulfate polystyrene latex of 55 nm were named Latex-1 and Latex-2 respectively.

4 DATA ANALYSIS

In this section, the nonexponentiality of $g^{(2)}(\tau)$ is investigated using the standard polystyrene latex and PNIPAM samples at different scattering angles.

4.1 Small particles

For small particles, the standard DLS technique can be used at any given scattering angle. For narrow particle size distributions, the effects of the form factor can be neglected, the particle size information obtained at different scattering angles should be the same. The particle sizes and distributions of the standard polystyrene latex samples Latex-1 and Latex-2 provided by the supplier are small and narrow respectively. The deviation between an exponentiality and $g^{(2)}(\tau)$ are investigated at a temperature of 298.5 K and scattering angles 30°, 40°, 50°, 60°, 70°, 80°, 90°, 100°, 120°, 130°, 140° and 150°, respectively. The logarithm of the DLS data $\ln(g^{(2)}(\tau) - 1)$ was plotted as a function of the delay time τ , respectively. The results for Latex-1 and Latex-2 measured at scattering angles 30°, 60°, 90°, 120° and 150° are shown in Figs. 1a and 1b respectively. Figure 1 shows clearly the nonexponentiality of $g^{(2)}(\tau)$ at a given scattering angle investigated is small. The values of apparent hydrodynamic radius obtained at different scattering angles almost are equal. For Latex-1 and Latex-2, the values are about 37.27 nm and 64.5 nm respectively.

For PNIPAM samples at high temperatures, the particle sizes and distributions obtained using the SLS technique are small and narrow. The nonexponentiality of $g^{(2)}(\tau)$ for PNIPAM samples at high temperatures are investigated as the standard polystyrene latex samples Latex-1 and Latex-2 at a temperature of 298.5 K. The results for PNIPAM-1 and PNIPAM-2 at about a temperature of 312.6 K and scattering angles 30°, 60°, 90°, 120° and 150° are shown in Figs. 2a and 2b respectively. Figure 2 shows clearly the nonexponentiality of $g^{(2)}(\tau)$ at a given scattering angle investigated is small. The values of apparent hydrodynamic radius obtained at different scattering angles almost are equal. For PNIPAM-1 and PAIPAM-2, the values are about 137.8 nm and 136.5 nm respectively.

4.2 Large particles

For large particles, since most of scattering light is cancelled due to the light interference in the vicinity of the scattered intensity minimum and the scattered

intensity at large scattering angles is influenced by the reflected light, the information included in DLS data is complex. In order to avoid the considerations for the situations, the nonexponentiality of $g^{(2)}(\tau)$ is investigated at small scattering angles before the emergence of the scattered intensity minimum. For the samples PNIPAM-1 and PANIPAM-2 at a temperature of 302.2 K, the scattered intensity minimums emerge at about the scattering angles 85° and 97° respectively, the deviations between an exponentiality and $g^{(2)}(\tau)$ are explored before the scattering angle 75° . The logarithm of the DLS data $\ln(g^{(2)}(\tau) - 1)$ was plotted as a function of the delay time τ . The results for PNIPAM-1 and PNIPAM-2 at scattering angles 30° , 50° and 70° are shown in Figs. 3a and 3b respectively. Figure 3 shows clearly the nonexponentiality of $g^{(2)}(\tau)$ at a given scattering angle investigated is small. The values of apparent hydrodynamic radius are a function of the scattering angle. For PNIPAM-1 the values are about 320 nm to 310 nm and for PNIPAM-2 the values are from 300 nm to 295 nm during scattering angle range from 30° to 70° .

5 RESULTS AND DISCUSSION

Because the distributions of the PNIPAM submicron and standard polystyrene latex samples are narrow and the expected values of the DLS data calculated based on the commercial and static particle size information are consistent with the experimental data [7, 8], the DLS simulated data were used in order to explore the effects of particle size distribution on the deviation between an exponentiality and $g^{(2)}(\tau)$ and the initial slope of the logarithm of $g^{(2)}(\tau)$ at different scattering angles in detail. The method that produces the DLS simulated data has been detailed before [7]. In this work, the number distribution of particle sizes is still chosen as a Gaussian distribution

$$G(R_s; \langle R_s \rangle, \sigma) = \frac{1}{\sigma\sqrt{2\pi}} \exp\left(-\frac{1}{2} \left(\frac{R_s - \langle R_s \rangle}{\sigma}\right)^2\right), \quad (8)$$

where $\langle R_s \rangle$ is the mean static radius and σ is the standard deviation related to the mean static radius.

The simulated data were produced using the information: the mean static radius $\langle R_s \rangle$, standard deviation σ , temperature T , viscosity of the solvent η_0 , scattering angle θ , wavelength of laser light λ , refractive index of the water n_s and constant $a = R_h/R_s$ were set to 50 nm, 10 nm, 300.49K, 0.8479 mPa·S, 90° , 632.8 nm, 1.332 and 1.1, respectively. When the data of $(g^{(2)}(\tau) - 1)/\beta$ were obtained, the 1% statistical noises were added and the random errors were set 3%. Five simulated data were produced respectively. The fit results for one of the DLS simulated data at different delay time ranges using Eq. 4 with $\mu_2 = 0$ and $\mu_2 \neq 0$ respectively are listed in Table 1.

The fit results of $\langle \Gamma \rangle$ and μ_2 are influenced by the delay time range being fit as shown in Table 1. When Eq. 4 was used to fit the simulated data produced based on the mean static radius 50 nm and standard deviation 10 nm at a scattering

Delay time (s)	$\langle\Gamma\rangle_{first} (s^{-1})$	χ^2	$\langle\Gamma\rangle_{two} (s^{-1})$	$\mu_2 (s^{-2})$	χ^2
$2*10^{-7}$ to 0.00151	1395.0±0.8	1.42	1420±3	46900± 4900	0.42
$2*10^{-7}$ to 0.00166	1390.2±0.7	2.79	1421±2	50500±3400	0.41
$2*10^{-7}$ to 0.00181	1389.6±0.6	2.86	1421±2	50300±3300	0.40
$2*10^{-7}$ to 0.00196	1386.4±0.6	3.92	1421±2	50100±2700	0.39
$2*10^{-7}$ to 0.00211	1384.7±0.5	4.51	1421±2	50200±2500	0.38
$2*10^{-7}$ to 0.00226	1374.1±0.4	9.63	1423±2	53300±1900	0.39
$2*10^{-7}$ to 0.00241	1373.3±0.3	9.72	1422±2	52400±1800	0.41

Table 1: The fit results of simulated data produced based on the mean static radius 50 nm, standard deviation 10 nm and a scattering angle of 90° at different delay time ranges using Eq. 4 with $\mu_2 = 0$ and $\mu_2 \neq 0$ respectively.

angle of 90° under the conditions of $\mu_2 = 0$ and $\mu_2 \neq 0$ respectively, it was found that the uncertainties in parameters decrease and $\langle\Gamma\rangle$ and μ_2 stabilize as the delay time range is increased. From Eq. 6, the relative width of the apparent hydrodynamic radius distribution is about 0.16. This value is equal to that of the relative width of the apparent hydrodynamic radius distribution obtained at a scattering angle of 30° [9] and different from the relative width of this simulated data 0.2. Fit results obtained using both procedures at the delay time range 2×10^{-7} to 0.00196 s are shown in Fig. 4. For both the fit results, the residuals $(y_i - y_{fit}) / \sigma_i$ are random as the delay time is changed, where y_i , y_{fit} and σ_i are the data, the fit value and the uncertainty in the data at a given delay time τ_i , respectively.

The fit results for other particle size distributions also have been analyzed. The simulated data were produced using the same temperature T , viscosity of the solvent η_0 , wavelength of laser light λ , mean static radius $\langle R_s \rangle$, constant a and refractive index of the water n_s . The standard deviations and scattering angles θ were set to 3 nm, 5 nm, 15 nm, 20 nm and 25 nm and 60°, 90°, 120° and 150°, respectively. Since the standard method of cumulants obtains the distribution of apparent hydrodynamic radius from the deviation between an exponentiality and $g^{(2)}(\tau)$ at a single scattering angle, the simulated data were used to investigate the effects of the particle size distributions on the nonexponentiality of $g^{(2)}(\tau)$ at different scattering angles. The logarithm of the simulated data produced without noises and errors was plotted as a function of the delay time τ . All results for the standard deviations 3 nm, 10 nm, 20 nm, 25 nm and mean static radius 50 nm are shown in Fig. 5a for a scattering angle of 90° and in Fig. 5b for a scattering angle of 150°. Figure 5 shows the effects of the standard deviation are small on the nonexponentiality of $g^{(2)}(\tau)$ and large on the initial slope of the logarithm of $g^{(2)}(\tau)$ $\langle\Gamma\rangle$ at scattering angles 90° and 150°.

Since the particle size is an important quantity obtained using the DLS technique, the effects of the particle size distribution on the apparent hydrodynamic radius were thus investigated. The values of the apparent hydrodynamic radius

$\sigma/\langle R_s \rangle$	Scattering angle 90°			Scattering angle 150°		
	$R_{h,app1}$ (nm)	$R_{h,app2}$ (nm)	R_{cal} (nm)	$R_{h,app1}$ (nm)	$R_{h,app2}$ (nm)	R_{cal} (nm)
0.06	56.1±0.2	56.1±0.1	56.0	56.0±0.1	55.8±0.6	56.0
0.1	57.8±0.2	57.2±0.6	57.7	57.8±0.2	57.6±0.6	57.5
0.2	65.1±0.1	64.3±0.5	64.7	64.3±0.4	63.1±0.4	64.0
0.3	74.4±0.5	72.6±0.6	73.8	72.6±0.5	70.4±0.6	72.2
0.4	84.7±0.5	82.1±0.7	83.7	81.5±0.3	79±1.	80.5
0.5	94.6±0.4	90.7±0.8	93.53	90.2±0.5	86.3±0.9	88.7

Table 2: Values of $R_{h,app}$ obtained using Eqs. 4 and 5 with $\mu_2 = 0$ and $\mu_2 \neq 0$, and Eq. 7 for the simulated data produced using the mean static radius 50 nm and different standard deviations at scattering angles 90° and 150°, respectively.

obtained using Eqs. 4 and 5 with $\mu_2 = 0$ and $\mu_2 \neq 0$, and Eq. 7 respectively for the simulated data produced using the mean static radius 50 nm and different standard deviations at scattering angles 90° and 150° are shown in Table 2. From the relationship $a = R_h/R_s = 1.1$, the mean hydrodynamic radius $\langle R_h \rangle$ is 55 nm.

The results in Table 2 show that the value of the apparent hydrodynamic radius is greatly influenced by the particle size distribution. The part of apparent hydrodynamic radius represents the effects of particle size distributions. The wider the particle size distribution, the larger the value of the apparent hydrodynamic radius. The consistency between the value calculated from Eq. 7 and the result obtained using the first cumulant also shows the deviations between the exponentiality and $g^{(2)}(\tau)$ at scattering angles 90° and 150° respectively are small even for very wide distribution like the relative width distribution 50%. The difference between the results obtained using the first and first two cumulants is influenced by the particle size distribution. For narrow distributions, they are almost equal. For a wide distribution like 50%, the difference is less than 5%. The relative width of apparent hydrodynamic radius obtained from the deviation between an exponentiality and $g^{(2)}(\tau)$ is about 24% at a scattering angle of 90° and 27% at a scattering angle of 150° for the simulated data produced using the relative width of hydrodynamic radius 50%.

Comparing the results of apparent hydrodynamic radius obtained at scattering angles 30° [9], 90° and 150°, for narrow particle size distributions the values of apparent hydrodynamic radius almost do not depend on the scattering angle and for wide particle size distributions the values are a function of the scattering angle. However, for any situation of the simulated data produced using the mean static radius 50 nm, the deviations between an exponentiality and $g^{(2)}(\tau)$ are small. In order to explore the question further, the new simulated data were produced using the same temperature T , viscosity of the solvent η_0 , wavelength of laser light λ and refractive index of the water n_s . The mean static radius $\langle R_s \rangle$ and constant a were set to 120 nm and 1.2 respectively. The standard deviations and scattering angles were set to 8, 12, 24, 36, 48, 60 nm and 30°,

$\sigma/\langle R_s \rangle$	$R_{h,app1} (nm)$	$R_{h,app2} (nm)$	$R_{cal} (nm)$
0.07	146.3±0.2	146.7±0.7	145.9
0.1	148.5±0.3	148±1	148.2
0.2	158.9±0.8	156.9±0.8	157.7
0.3	168.5±0.7	164.2±0.9	167.0
0.4	175.7±0.9	170.±1.	174.1
0.5	184.0±0.7	177±2	181.7

Table 3: Values of $R_{h,app}$ obtained using Eqs. 4 and 5 with $\mu_2 = 0$ and $\mu_2 \neq 0$, and Eq. 7 for the simulated data produced using the mean static radius 120 nm and different standard deviations at a scattering angle of 90° .

60° , 90° , 120° , 150° , respectively.

The simulated data were thus used to explore the nonexponentiality of $g^{(2)}(\tau)$ at different scattering angles. The logarithm of the simulated data produced without noises and errors was plotted as a function of the delay time τ . All results at scattering angles 30° and 90° for the standard deviations 8 nm, 24 nm, 48 nm, 60 nm and mean static radius 120 nm are shown in Figs. 6a and 6b respectively. Figure 6 shows the effects of the standard deviation are small on the nonexponentiality of $g^{(2)}(\tau)$ and large on the initial slope of the logarithm of $g^{(2)}(\tau)$ $\langle \Gamma \rangle$ at scattering angles 30° and 90° .

The effects of the particle size distribution on the apparent hydrodynamic radius were thus explored at a scattering angle of 90° . The values of the apparent hydrodynamic radius obtained using Eqs. 4 and 5 with $\mu_2 = 0$ and $\mu_2 \neq 0$, and Eq. 7 respectively for the simulated data produced using the mean static radius 120 nm and different standard deviations are shown in Table 3. From the relationship $a = R_h/R_s = 1.2$, the mean hydrodynamic radius $\langle R_h \rangle$ is 144 nm.

The results in Table 3 also show that the value of the apparent hydrodynamic radius is greatly influenced by the particle size distribution. The part of apparent hydrodynamic radius represents the effects of particle size distributions. The wider the particle size distribution, the larger the value of the apparent hydrodynamic radius. The consistency between the value calculated from Eq. 7 and the result obtained using the first cumulant also shows the deviations between the exponentiality and $g^{(2)}(\tau)$ at a scattering angle of 90° are small even for very wide distribution like the relative width distribution 40%, respectively. The relative width of apparent hydrodynamic radius obtained from the deviation between an exponentiality and $g^{(2)}(\tau)$ is about 27% for the simulated data produced using the relative width of hydrodynamic radius 50% at a scattering angle of 30° and 26% at a scattering angle of 90° . Meanwhile, according to Eq. 1, the apparent hydrodynamic radius obtained using the cumulants method is a function of the scattering angle. In order to investigate the effects of the scattering angle on the apparent hydrodynamic radius, the initial slopes of $g^{(2)}(\tau)$ at different scattering angles were divided by the square of the scattering vectors respectively. The results for the simulated data produced based

on the mean static radius 50 nm with the standard deviations 3 nm, 10 nm and 25 nm and for the simulated data produced based on the mean static radius 120 nm with the standard deviations 8 nm, 24 nm and 60 nm at scattering angles 30°, 90° and 150° are shown in Figs. 7a and 7b, respectively. Figure 7a shows the values of the apparent hydrodynamic radius do not depend on the scattering angle for the simulated data produced based on the mean static radius 50 nm with the standard deviations 3 nm and 10 nm, and are a function of the scattering angle for the simulated data obtained using the mean static radius 50 nm and standard deviation 25 nm. Figure 7b shows the values of the apparent hydrodynamic radius do not depend on the scattering angle for the simulated data obtained using the mean static radius 120 nm and standard deviation 8 nm and are a function of the scattering angle for the simulated data produced based on the mean static radius 120 nm and standard deviation 24 nm. Figure 7b also reveals that the value obtained from the simulated data produced using the mean static radius 120 nm and standard deviations 24 nm at a scattering angle of 150° is equal to that obtained from the simulated data produced based on the mean static radius 120 nm and standard deviations 8 nm and the nonexponentiality of the DLS data produced using the mean static radius 120 nm and standard deviation 60 nm is very large at a scattering angle of 150°.

In order to investigate further the effects of the scattering angle on the nonexponentiality of the DLS data produced using the static radius 120 nm and standard deviation 60 nm at scattering angles 30°, 60°, 90°, 120° and 150°, the plots of $\ln((g^{(2)}(\tau) - 1)/\beta)$ as a function of the delay time τ are shown in Fig. 8.

Figure 8 reveals the effects of the scattering angle on the nonexponentiality of the DLS data are large. At scattering angles 30° and 60°, the plots of $\ln((g^{(2)}(\tau) - 1)/\beta)$ as a function of the delay time τ are consistent with the lines respectively and at scattering angles 90°, 120° and 150°, the plots of $\ln((g^{(2)}(\tau) - 1)/\beta)$ as a function of the delay time τ deviate clearly from the lines respectively. According to Eq. 1, two terms $P(q, R_s)$ and $\exp(-q^2 D\tau)$ include the parameter of the scattering angle. In order to investigate the effects of the form factor on the deviation between an exponentiality and $g^{(2)}(\tau)$, $P(q, R_s)$ was set to 1. The simulated data were produced again at scattering angles 30°, 60°, 90°, 120° and 150°. $\ln((g^{(2)}(\tau) - 1)/\beta)$ was plotted as a function of the delay time τ , respectively. The results are shown in Fig. 9. Comparing Fig. 8 with Fig. 9, the nonexponentiality of the DLS data is influenced obviously by $P(q, R_s)$.

Figure 7 also reveals that the results obtained using the cumulants method from the DLS data cannot be determined even if the plots of $\ln((g^{(2)}(\tau) - 1)/\beta)$ as a function of the delay time τ are consistent with lines, respectively. For example, the values of apparent hydrodynamic radius are 219 ± 2 nm and 244 ± 2 nm at a scattering angle of 30° and 175.7 ± 0.9 nm and 184.0 ± 0.7 nm at a scattering angle of 90° for the simulated data produced based on the mean static radius 120 nm with the standard deviations 48 and 60 nm respectively. In

$\sigma / \langle R_s \rangle$	Scattering angle				
	0	30°	60°	90°	120°
0.06	55.98	55.97	55.94	55.91	55.87
0.1	57.65	57.62	57.55	57.45	57.35
0.2	64.62	64.51	64.22	63.81	63.40
0.3	74.15	73.90	73.22	72.27	71.30
0.4	85.03	84.56	83.28	81.48	79.67
0.5	96.63	95.84	93.69	90.71	87.74

Table 4: Values of $R_{h,app}$ obtained at different scattering angles for the simulated data produced based on the mean static radius 50 nm and different standard deviations using the intensity-weighted average diffusion coefficient.

order to eliminate the effects of the scattering angle, the value of apparent hydrodynamic radius can be obtained by approximating the scattering angle 0. The calculated values obtained using intensity-weighted average diffusion coefficient [6] were used to study this question in order to discuss simply. The apparent hydrodynamic radius is calculated using the following equation

$$R_{h,app} = \frac{\int R_s^6 P(q, R_s) G(R_s) dR_s}{\int R_s^6 P(q, R_s) G(R_s) / R_h dR_s}. \quad (9)$$

The values calculated using Eq. 9 are listed in Table 4 for the simulated data produced based on the mean static radius 50 nm and different standard deviations at scattering angles 0, 30°, 60°, 90° and 120°, respectively. The results show the values of apparent hydrodynamic radius are a function of the scattering angle and particle size distribution. Although the effects of the scattering angle are eliminated at a scattering angle of 0, the values of apparent hydrodynamic radius still are determined by the particle size distribution. Because the distribution of apparent hydrodynamic radius is obtained from the nonexponentiality of $g^{(2)}(\tau)$ related to the exponentiality of the average decay rate at a single scattering angle, the apparent hydrodynamic radius and its distribution obtained at a scattering angle of 0 are different from the hydrodynamic radius and its distribution.

6 CONCLUSION

The nonexponentiality of $g^{(2)}(\tau)$ is determined by the particle size distribution and scattering angle. In general, the effects of the particle size distribution are small on the deviation between an exponentiality and $g^{(2)}(\tau)$ and very large on the initial slope of the logarithm of $g^{(2)}(\tau)$ and the effects of the scattering angle are determined by the particle size distribution and mean particle size. Under some conditions, the nonexponentiality of $g^{(2)}(\tau)$ is greatly influenced by the scattering angle. The values of the apparent hydrodynamic radius are a function

of the particle size distribution and scattering angle. The wider the particle size distribution, the larger the value of the apparent hydrodynamic radius. The apparent hydrodynamic radius and its distribution obtained using the cumulants method are different from the hydrodynamic radius and its distribution.

Fig. 1. The differences between the lines and plots of $\ln((g^{(2)}(\tau) - 1))$ as a function of the delay time τ are explored at a temperature of 298.5 K and scattering angles 30°, 60°, 90°, 120° and 150°. The symbols show the experimental data and the lines show the linear fitting to the experimental data respectively. The results for Latex-1 and Latex-2 are shown in a and b respectively.

Fig. 2. The differences between the lines and plots of $\ln((g^{(2)}(\tau) - 1))$ as a function of the delay time τ are investigated at a temperature of 312.6 K and scattering angles 30°, 60°, 90°, 120° and 150°. The symbols show the experimental data and the lines show the linear fitting to the experimental data respectively. The results for PNIPAM-1 and PNIPAM-2 are shown in a and b respectively.

Fig. 3. The differences between the lines and plots of $\ln((g^{(2)}(\tau) - 1))$ as a function of the delay time τ are investigated at a temperature of 302.2 K and scattering angles 30°, 50° and 70°. The symbols show the experimental data and the lines show the linear fitting to the experimental data respectively. The results for PNIPAM-1 and PNIPAM-2 are shown in a and b respectively.

Fig. 4. The fit results of $g^{(2)}(\tau)$ for the simulated data produced based on the mean static radius 50 nm and standard deviations 10 nm at a scattering angle of 90°. The circles show the simulated data, the line represents the fit results obtained using Eq. 4 and the diamonds show the residuals $(y_i - y_{fit})/\sigma_i$. The results for $\mu_2 = 0$ and $\mu_2 \neq 0$ are shown in a and b respectively.

Fig. 5. The differences between the lines and plots of $\ln((g^{(2)}(\tau) - 1)/\beta)$ as a function of the delay time τ . The symbols show the simulated data and the lines show the linear fitting to the simulated data respectively. The results for the simulated data at scattering angles 90° and 150° are shown in a and b respectively.

Fig. 6. The differences between the lines and plots of $\ln((g^{(2)}(\tau) - 1)/\beta)$ as a function of the delay time τ . The symbols show the simulated data and the lines show the linear fitting to the simulated data respectively. The results for the simulated data at scattering angles 30° and 90° are shown in a and b respectively.

Fig. 7. The differences between the lines and plots of $\ln((g^{(2)}(\tau) - 1)/\beta)$ produced based on the mean static radius 50 nm with the standard deviations 3, 10 nm and 25 nm and 120 nm with the standard deviations 8 nm, 24 nm and 60 nm at the scattering angles 30°, 90° and 150° as a function of the delay time τ , respectively. The symbols show the simulated data and the lines show the linear fitting to the simulated data respectively. The results for the simulated data produced using the mean static radii 50 nm and 120 nm are shown in a and b respectively.

Fig. 8. The differences between the lines and plots of $\ln((g^{(2)}(\tau) - 1)/\beta)$ produced based on the mean static radius 120 nm and standard deviation 60 nm

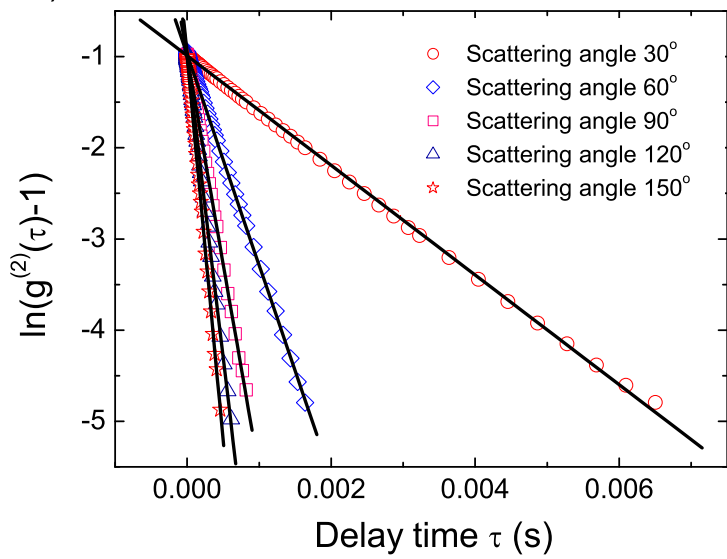
at the scattering angles 30° , 60° , 90° , 120° and 150° as a function of the delay time τ , respectively. The symbols show the simulated data. The results for the simulated data at different scattering angles are shown in a and b respectively.

Fig. 9. The differences between the lines and plots of $\ln((g^{(2)}(\tau) - 1)/\beta)$ produced based on the mean static radius 120 nm and standard deviation 60 nm at the scattering angles 30° , 60° , 90° , 120° and 150° as a function of the delay time τ assuming $P(q, R_s) = 1$, respectively. The symbols show the simulated data and the lines show the linear fitting to the simulated data respectively. The results for the simulated data at different scattering angles are shown in a and b respectively.

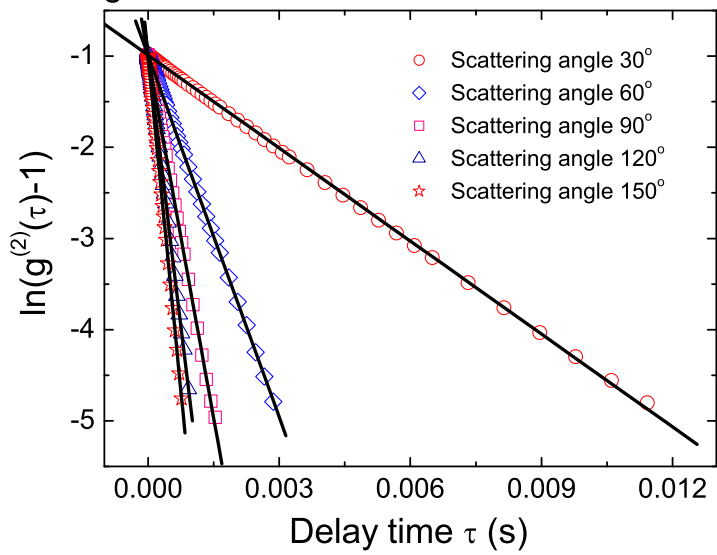
References

- [1] D. E. Koppel, J. Chem. Phys. **57**, 4814(1972).
- [2] C. B. Barger, J. Chem. Phys. **61**, 2134(1974).
- [3] J. C. Brown, P. N. Pusey and R. Dietz, J. Chem. Phys. **62**, 1136(1975).
- [4] B. J. Berne and R. Pecora, *Dynamic Light Scattering* (Robert E. Krieger Publishing Company, Malabar, Florida, 1990).
- [5] G. Bryant, S. Martin, A. Budi and W. van Meegen, Langmuir **19**, 616(2003).
- [6] P. N. Pusey and W. van Meegen, J. Chem. Phys. **80**, 3513(1984).
- [7] Y. Sun arxiv.org/abs/physics/0511159.
- [8] Y. Sun arxiv.org/abs/physics/0511160.
- [9] Y. Sun arxiv.org/abs/physics/0511161.
- [10] The ALV Manual of the Version for ALV-5000/E for Windows, ALV-GmbH, Germany, 1998.

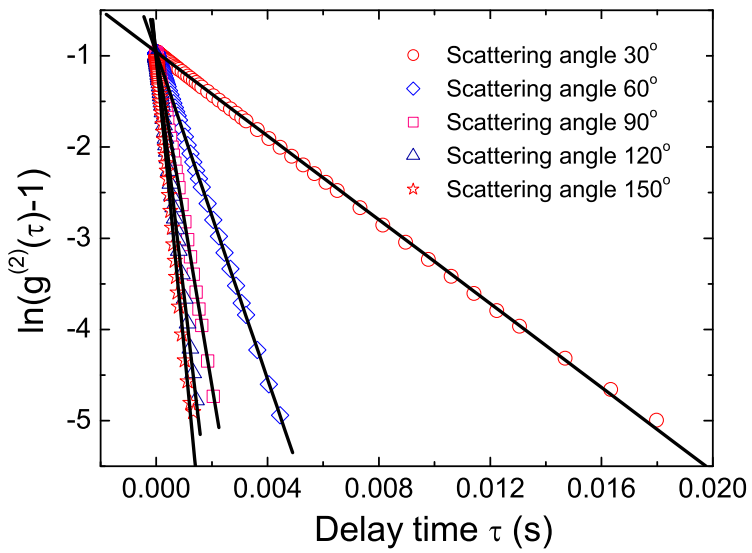
a). Fig. 1



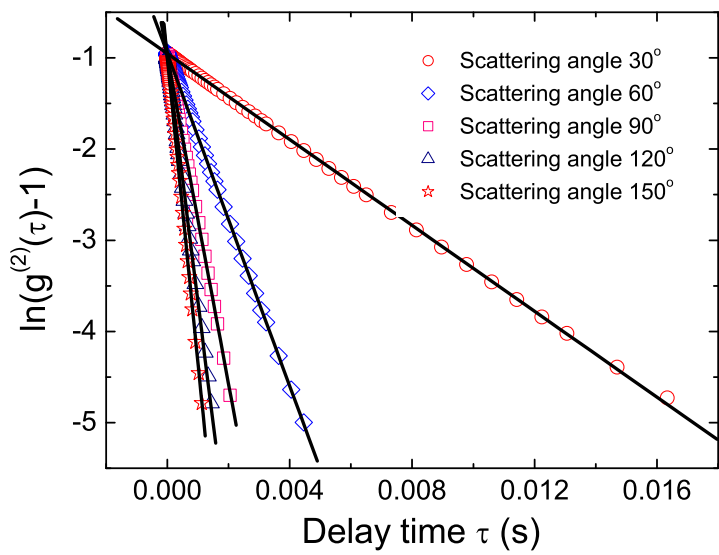
b). Fig. 1

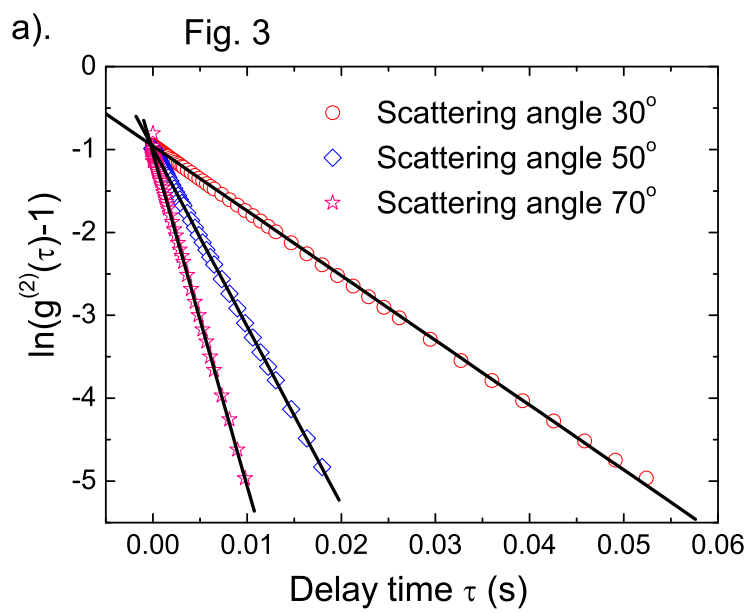


a). Fig. 2.

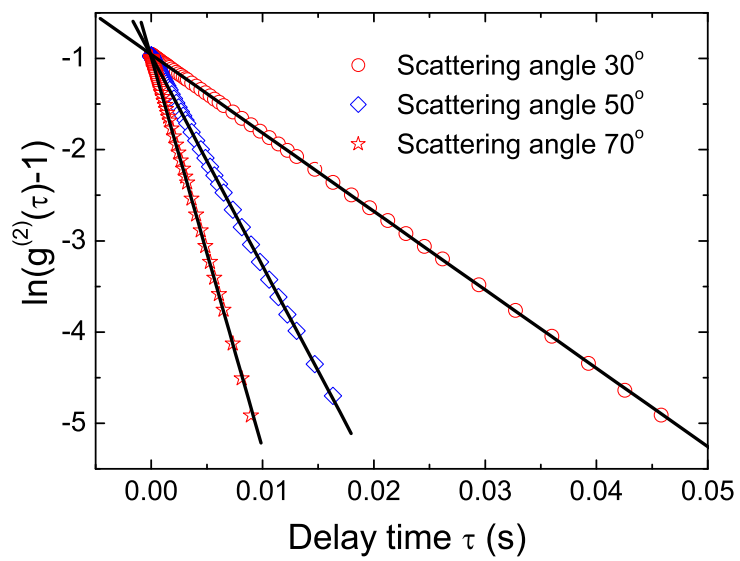


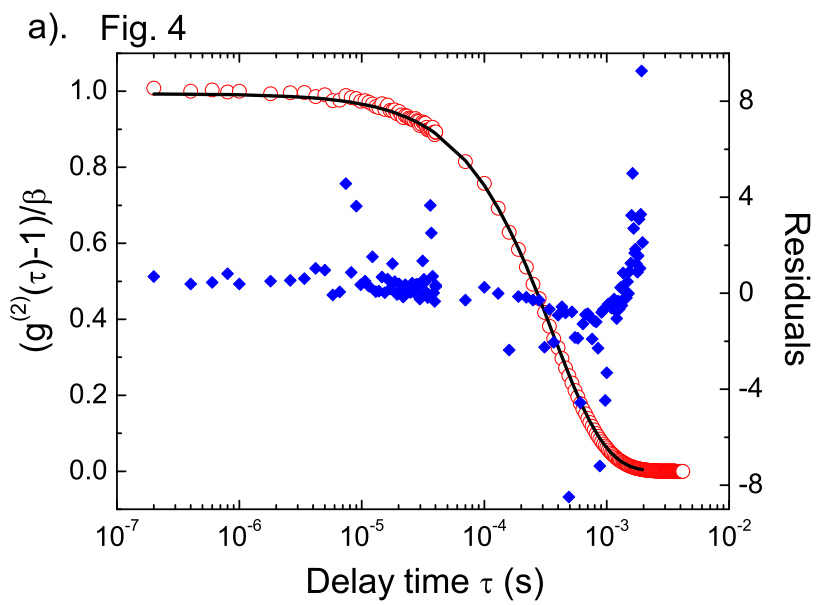
b). Fig. 2



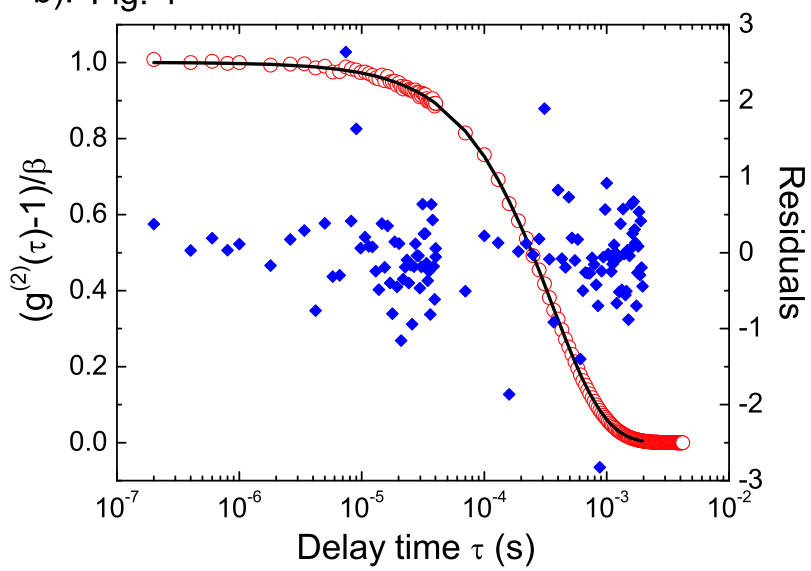


b). Fig. 3

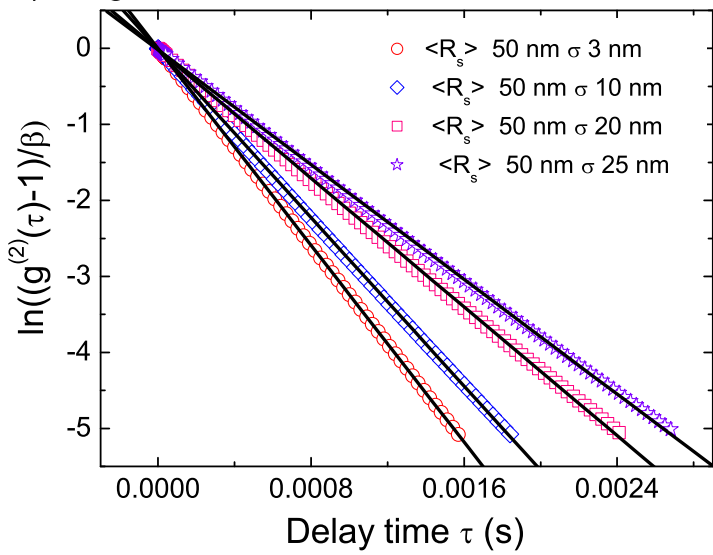




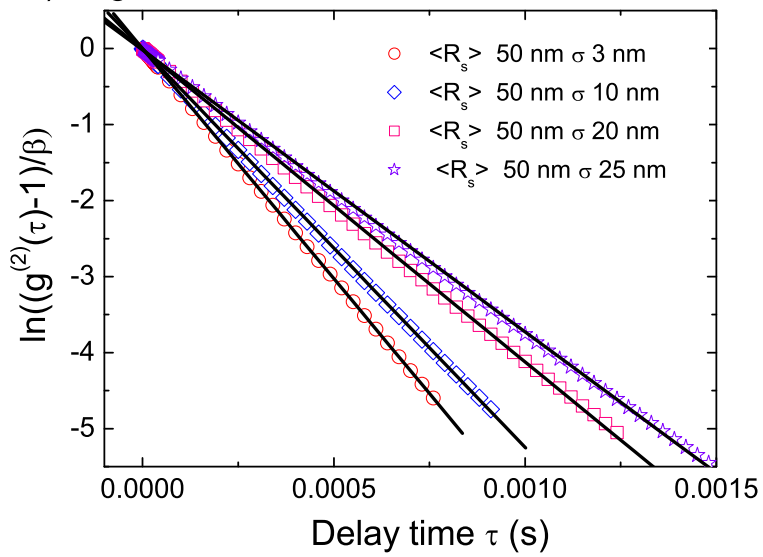
b). Fig. 4



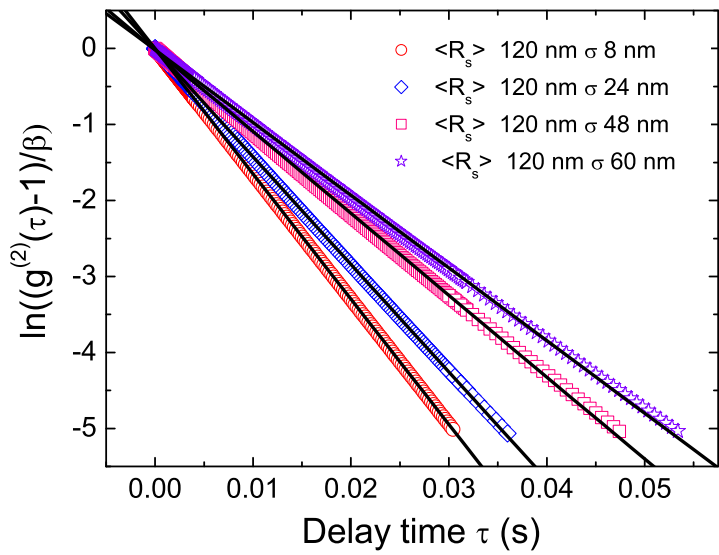
a). Fig. 5



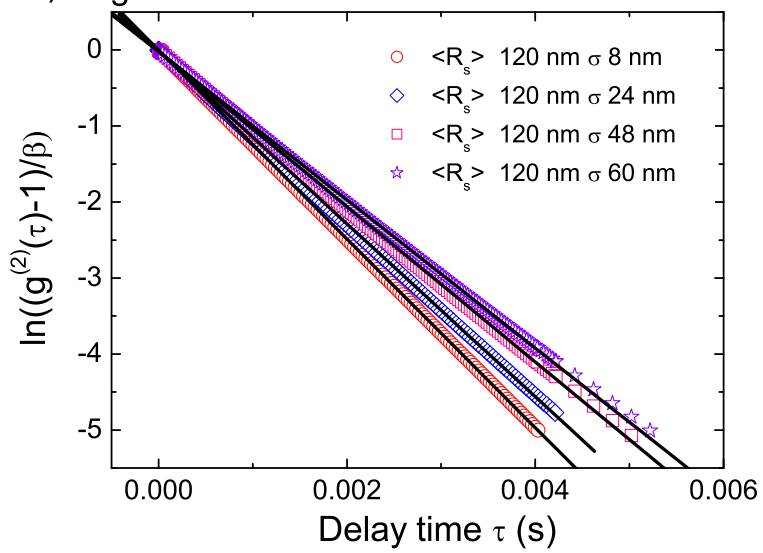
b). Fig. 5

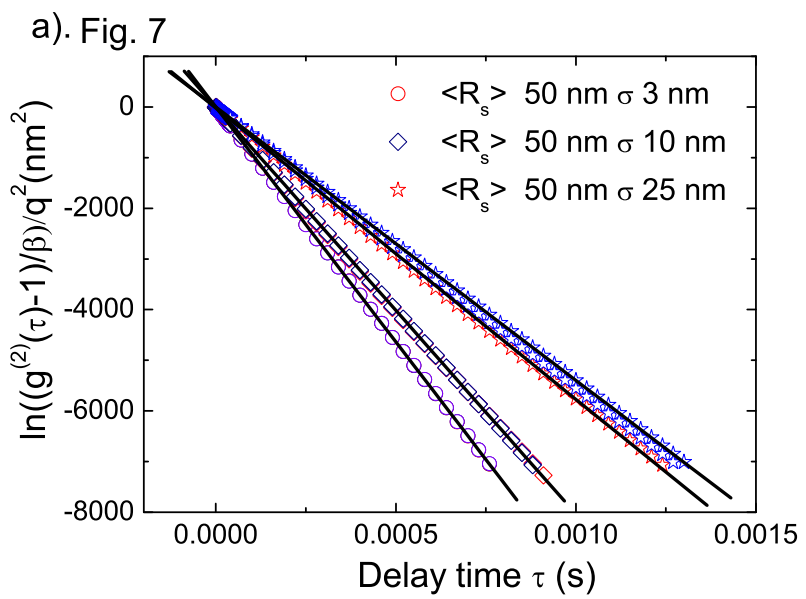


a). Fig. 6

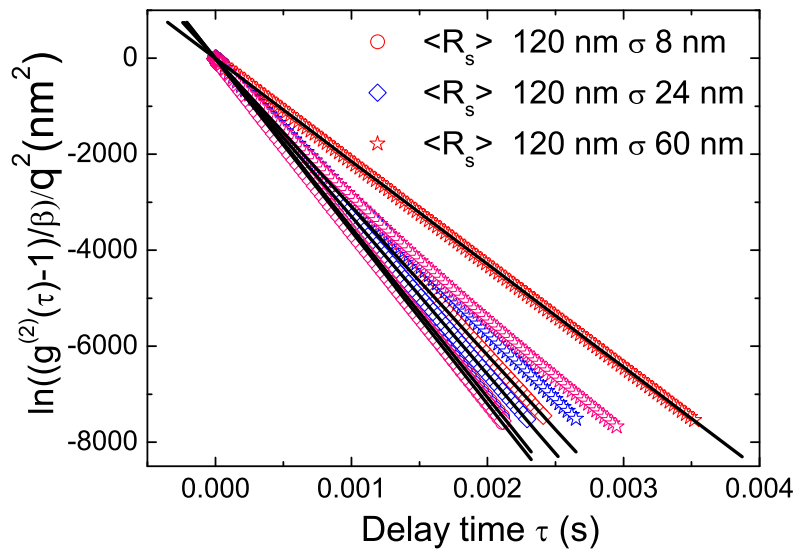


b). Fig. 6

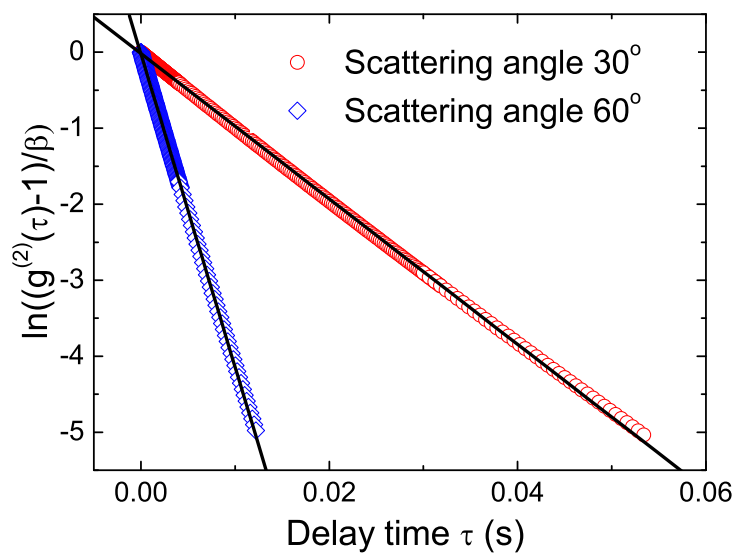




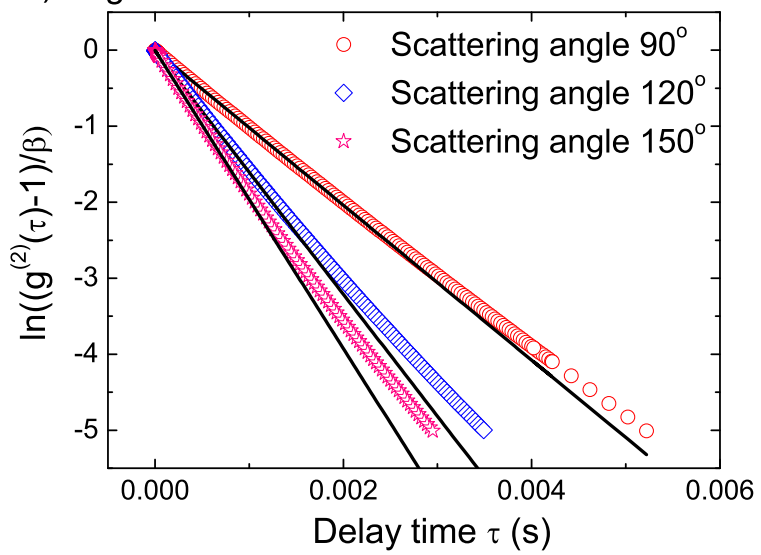
b). Fig. 7



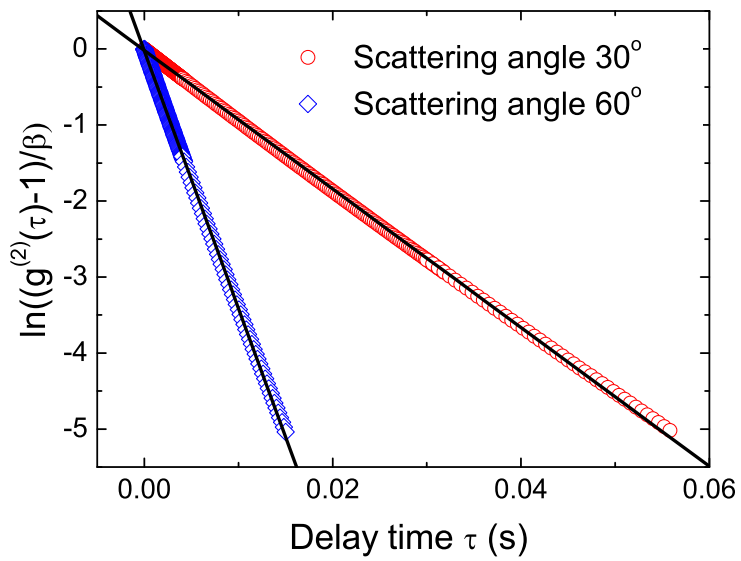
a). Fig. 8



b). Fig. 8



a). Fig. 9



b). Fig. 9

